ACS APPLIED MATERIALS & INTERFACES
Research Article
Cite This: ACS Appl. Mater. Interfaces 2018, 10, 29505−29510
www.acsami.org

Seeding Iron Trifluoride Nanoparticles on Reduced Graphite Oxide for Lithium-Ion Batteries with Enhanced Loading and Stability

Dantong Qiu,[†,‡] Liangjie Fu,[§] Chun Zhan,[∥] Jun Lu,*[,∥] and Di Wu*[,†,‡,⊥,#]

[†]Alexandra Navrotsky Institute for Experimental Thermodynamics, [‡]Materials Science and Engineering, [⊥]The Gene and Linda Voiland School of Chemical Engineering and Bioengineering, and [#]Department of Chemistry, Washington State University, Pullman, Washington 99163, United States

[§]Centre for Mineral Materials, School of Minerals Processing and Bioengineering, Central South University, Changsha, Hunan 410083, China

[∥]Chemical Sciences and Engineering Division, Argonne National Laboratory, Argonne, Illinois 60439, United States

ABSTRACT: Development of electric vehicles and portable electronic devices during the past decade calls for lithium-ion batteries (LIBs) with enhanced energy density and higher stability. Integration of FeF_3 phases and carbon structures leads to promising cathode materials for LIBs with high voltage, capacity, and power. In this study, $FeF_3 \cdot 0.33H_2O$ nanoparticles were synthesized on reduced graphite oxide (rGO) nanosheets using an in situ approach. By chemically tuning the interfacial bonding between $FeF_3 \cdot 0.33H_2O$ and rGO, we successfully achieved high particle loading and enhanced cycling stability. Specifically, a discharge capacity of ∼208.3 mAh g^{-1} was observed at a current density of 0.5 C. The $FeF_3 \cdot 0.33H_2O$/rGO nanocomposites also demonstrate great cycle capability with a reversible discharge capacity of 133.1 mAh g^{-1} after 100 cycles at 100 mA g^{-1}; the capacity retention is about 97%. This study provides an alternative strategy to further improve the stability and performance of iron fluoride/carbon nanocomposite materials for LIB applications.

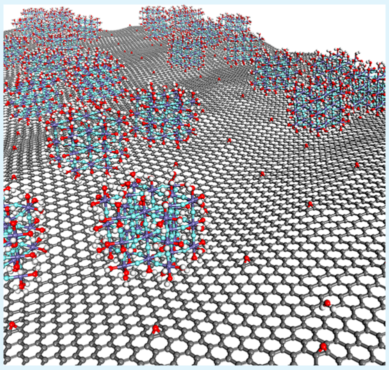

KEYWORDS: *iron trifluoride, graphite oxide, lithium-ion battery, material stability, in situ synthesis, nanocomposite*

INTRODUCTION

Rapid development of electric vehicles (EVs) and portable electronic devices requiring batteries with higher energy density and material stability has outran the current lithium-ion battery (LIB) technology.[1−3] The energy density of LIBs is mainly governed by the specific capacity and redox potential of the electrode materials. Increasing the capacity of the cathode materials is effective to enhance the energy density of LIBs.[3,4] Recently, special attention is given to metal fluorides owing to their high specific capacity and reaction voltage[5−10] among which iron fluoride (FeF_3) phases have shown great potential to qualify as a practically applicable LIB cathode material because of its higher safety rating (no oxygen) and much lower cost compared with $LiCoO_2$.[11−13] Additionally, for FeF_3 structures, once three-electron reactions occur, they can deliver a high energy density of as much as ∼1951 Wh kg^{-1}.[5,14−16] Even if a one-electron reaction takes place, compared with $LiCoO_2$, FeF_3 shows a higher theoretical energy density of 700 Wh kg^{-1}.[17] Moreover, intrinsically, FeF_3 features a high electromotive force (EMF) of 2.7 V and a theoretical capacity of 237 mAh g^{-1} with a one-electron transfer.[16]

Despite such advantages, one hurdle to overcome before successful practical application of FeF_3 in LIBs is its poor electric conductivity due to the highly ionic Fe−F bond. Multiple strategies, such as FeF_3 nanoparticle (NP) size reduction[18−20] and FeF_3−conductive material composite fabrication,[17,21] have been developed to meet this challenge. Architecting nanocomposites by coupling FeF_3 NPs with conductive materials, including carbon nanotubes,[22,23] porous carbon,[24] and conductive polymers,[25] is tested to be effective. Among the carbon materials, reduced graphene oxide (rGO) or graphene stands out owing to outstanding conductivity and mechanical properties.[26−30] So far, numerous FeF_3/graphene structures have been reported.[14,31−37] One study performed by Liu et al. in 2013 inspires our present study,[33] in which the authors directly employ graphene as the FeF_3 NP support. Specifically, a graphene dispersion was mixed with a hydrofluoric acid solution (HF) prior to the introduction of Fe^{3+} ions to create defects for nucleation of $FeF_3 \cdot 3H_2O$ nanocrystals with uniform size and morphology. After calcination, the final product, FeF_3/graphene, has a FeF_3 loading of 80 wt % and shows a specific capacity of 210 mAh g^{-1} at a current density of 0.3 C.[33]

Herein, we used an in situ approach to synthesize $FeF_3 \cdot 0.33H_2O$/rGO nanocomposites, in which Fe^{3+} was introduced to a graphite oxide (GO) dispersion, instead of graphene, prior to addition of other chemicals. The strong affinity between the Fe^{3+} cation and the highly concentrated oxygen-containing site (defect) on the GO surface resulted in “on-site” nucleation,

Received: May 23, 2018
Accepted: August 9, 2018
Published: August 9, 2018

DOI: 10.1021/acsami.8b08526

growth and precipitation of small $FeF_3{\cdot}0.33H_2O$ NPs up to high particle loading, and enabled strong $FeF_3{\cdot}0.33H_2O$ particle−rGO sheet interfacial bonding upon reduction. Such a synthesis strategy leads to (1) a significantly higher $FeF_3{\cdot}0.33H_2O$ loading on rGO (92.3 wt %); (2) an outstanding discharge capacity of ~208.3 mAh g^{-1} at a current density of 0.5 C; (3) an excellent cycle capability with highly reversible discharge capacity of 133.1 mAh g^{-1} after 100 cycles at 1000 mA g^{-1}; and (4) a high capacity retention, as much as 97%.

■ EXPERIMENTAL METHODS

Material Synthesis. A modified Hummer's method was applied to prepare the GO dispersion, in which 5.0 mg mL^{-1} nanoGO was dispersed in water under ultrasonication for 30 min resulting in a solution with a brownish color. To synthesize the $FeF_3{\cdot}0.33H_2O$/rGO nanocomposites, 10 mL of as-made GO dispersion was added into 100 mL of tetraethylene glycol, which was subjected to water removal at 100 °C for 2 h under constant stirring followed by cooling down to 50 °C. Then, 5 mmol of iron acetylacetonate, $Fe(acac)_3$, was introduced into this mixture maintained at 50 °C under stirring. Subsequently, 3 mL of hydrofluoric acid (40 wt % HF aqueous solution) was gradually dripped into the solution. Upon constant stirring at 50 °C for 16 h, the solid material was separated, washed with ethanol 5 times, and calcined at 220 °C under vacuum for 12 h to yield the final product, $FeF_3{\cdot}0.33H_2O$/rGO nanocomposite. Unsupported $FeF_3{\cdot}0.33H_2O$ NPs were also synthesized for comparison.

Characterization of Materials. Powder X-ray diffraction (XRD) patterns of as-prepared unsupported $FeF_3{\cdot}0.33H_2O$ NPs and $FeF_3{\cdot}0.33H_2O$/rGO nanocomposites were recorded at room temperature using a Bruker AXS D8 Advance X-ray diffractometer (40 kV, 40 mA, Cu Kα, λ = 1.5406 Å). Data were recorded from 10° to 80° with a step of 0.02° and 1 step s^{-1}. Raman spectroscopy (LabRAM HR Evolution, 532 nm laser) was performed to reveal the structural fingerprint of the as-prepared samples. The sample morphology was examined by scanning electron microscopy (SEM, Zeiss, Merlin, 5 keV) and transmission electron microscopy (TEM, Hitachi, H-7650, 80 keV). X-ray photoelectron spectroscopy (XPS) was performed on a PHI Quantera SXM spectrometer equipped with a monochromatic Al Kα radiation source. Calibration of the XPS binding energy scale was carried out based on the C 1 s peak at 284.8 keV.

Electrochemical Measurements. All electrodes tested were prepared by coating slurries containing $FeF_3{\cdot}0.33H_2O$/rGO active material (80 wt %), polyvinylidene fluoride (10 wt %), and carbon black (10 wt %) on an aluminum foil current collector. Subsequently, the electrodes were dried in a vacuum oven at 100 °C for 12 h. CR2025 coin cells were assembled in a glovebox (argon-filled with oxygen and moisture below 1 ppm). Lithium foil was used as the counter electrode. $LiPF_6$ solution (1 M) in ethylene carbonate−ethyl methyl carbonate−dimethyl carbonate (1:1:1 v/v/v) was chosen to be the electrolyte. The galvanostatic charge−discharge cycling performance was evaluated using a battery test system (NEWARE-BTS) operated from 1.8 to 4.5 V versus Li/Li^+ at various scan rates, ranging from 0.1 to 2 A g^{-1}. In addition, three-electrode cells (ECC-REF model, EL-CELL) with lithium foil as both the reference and counter electrodes were assembled for electrochemical impedance spectroscopy (EIS) tests employing a PARSTAT2273 electrochemical workstation (AMETEK). The electrical AC potential was controlled with an amplitude of 5 mV and a frequency ranging from 100 to 0.1 kHz.

■ RESULTS AND DISCUSSIONS

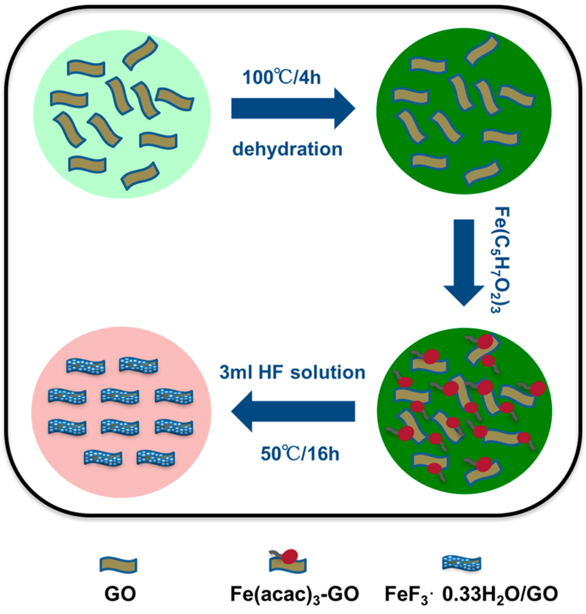

Figure 1. Schematic of the $FeF_3{\cdot}0.33H_2O$/rGO preparation process.

The preparation process of the $FeF_3{\cdot}0.33H_2O$/rGO nanocomposites is presented in Figure 1. Because of its high surface defect concentration and great dispersibility in polar solvents, such as water or ethanol, GO was selected as the carbon layer precursor instead of graphene. Fe^{3+} could be easily "seeded" onto the GO surface sites (defects), at which further introduction of HF solution directly led to $FeF_3{\cdot}0.33H_2O$ nucleation, growth, and precipitation. Subsequently, the as-made $FeF_3{\cdot}0.33H_2O$/GO was reduced to $FeF_3{\cdot}0.33H_2O$/rGO through calcination under vacuum for 12 h. Thermogravimetric analysis (not shown) suggests a high $FeF_3{\cdot}0.33H_2O$ particle loading of 92.3 wt %.

The XRD data of the unsupported $FeF_3{\cdot}0.33H_2O$ NPs and $FeF_3{\cdot}0.33H_2O$/rGO are shown in Figure 2a. The positions of the peaks suggest a hexagonal-tungsten-bronze type $FeF_3{\cdot}0.33H_2O$ phase (JCPDS card no. 76-1262) with grain sizes of 18.7 and 18.0 nm for the unsupported $FeF_3{\cdot}0.33H_2O$ NPs and $FeF_3{\cdot}0.33H_2O$/rGO, respectively. No detectable signal corresponding to rGO was observed.

The Raman spectra of GO and $FeF_3{\cdot}0.33H_2O$/rGO are presented in Figure 2b. The two well-resolved peaks observed at 1340 and 1580 cm^{-1} are attributed to the D- and G-bands, respectively. Typically, the D-band corresponds to structural disorder and surface defects that lead to symmetry interruption (breaking), while the G-band is attributed to first-order scattering of carbon domains, representing the highly ordered repeating sp^2 unit of GO. Therefore, I_D/I_G, the relative intensity of the D- and G-bands, is a reliable indicator of the degree of defects, the structural disorder, and the formation of new chemical bonds. In this study, the magnitude of I_D/I_G for $FeF_3{\cdot}0.33H_2O$/rGO (1.25) is significantly higher than that of pristine GO (0.97). This strongly suggests that the $FeF_3{\cdot}0.33H_2O$ NP−rGO interfacial bonds significantly increase the degree of disorder of the rGO surface leading to a symmetry break for the sp^2 carbon.

XPS experiments were conducted to further reveal the local bonding environment of C atoms (see Figure 3). The C 1s spectra of GO and $FeF_3{\cdot}0.33H_2O$/rGO suggest four types of carbon bonds. Specifically, they are C—C/C═C at 284.8 eV, C—O at 286.7 eV, C═O at 287.2 eV, and COOH at 288.7 eV. The carbon bond intensities of $FeF_3{\cdot}0.33H_2O$/rGO at 286.7, 287.2, and 288.7 eV are much weaker than the corresponding signals of GO. This is consistent with the

DOI: 10.1021/acsami.8b08526
ACS Appl. Mater. Interfaces 2018, 10, 29505−29510

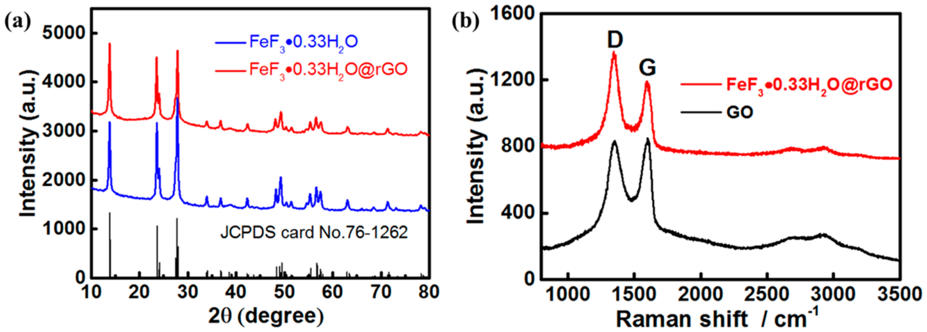

Figure 2. (a) XRD patterns and (b) Raman spectra of $FeF_3{\cdot}0.33H_2O$/rGO and the unsupported $FeF_3{\cdot}0.33H_2O$ NPs.

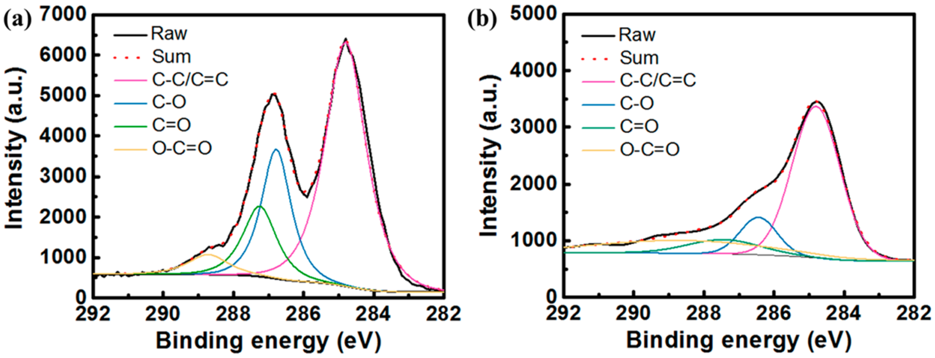

Figure 3. XPS spectra of carbon of (a) GO and (b) $FeF_3{\cdot}0.33H_2O$/rGO.

Raman spectroscopy results and suggests that the GO is reduced after calcination under vacuum.

SEM and TEM images of $FeF_3{\cdot}0.33H_2O$/rGO are presented in Figure 4. Monodispersed $FeF_3{\cdot}0.33H_2O$ nanospheres (∼150 nm) are observed with homogeneous distribution on the rGO layers. Figure 5 shows the TEM image of the unsupported $FeF_3{\cdot}0.33H_2O$ NPs. Interestingly, the particle size of the unsupported $FeF_3{\cdot}0.33H_2O$ NPs appears to be significantly larger than that of the $FeF_3{\cdot}0.33H_2O$/rGO nanocomposites. This highlights the critical role of rGO governing the size and morphology of the $FeF_3{\cdot}0.33H_2O$ NPs on rGO. Other than acting as a conductive network to enhance electron transfer, rGO also enables strong interfacial interactions inhibiting $FeF_3{\cdot}0.33H_2O$ NP aggregation.

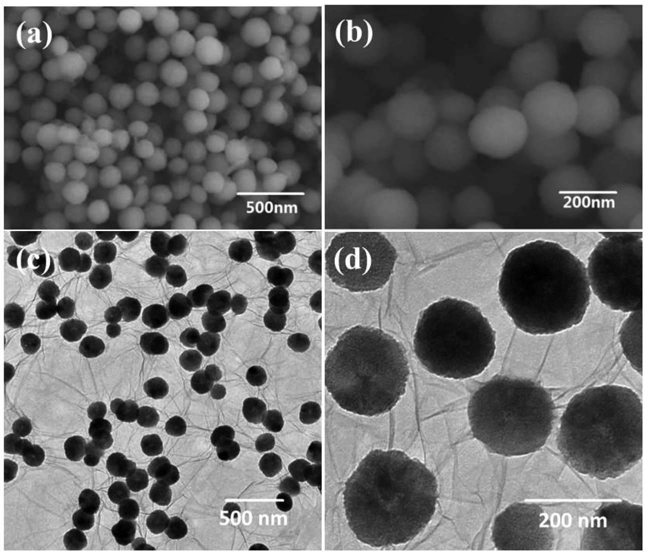

Figure 4. (a, b) SEM and (c, d) TEM images of $FeF_3{\cdot}0.33H_2O$/rGO.

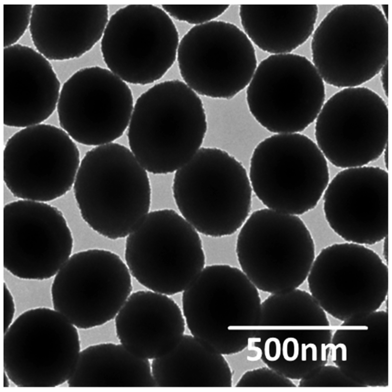

Figure 5. TEM image of unsupported $FeF_3{\cdot}0.33H_2O$ NPs.

The electrochemical performance of $FeF_3{\cdot}0.33H_2O$/rGO as a LIB cathode material was evaluated by galvanostatic tests carried out at 100 mA g^{-1}. The specific capacity was calculated on a mass basis of $FeF_3{\cdot}0.33H_2O$/rGO. Figure 6 presents the initial charge−discharge curves as the voltage increases from 1.8 to 4.5 V. The initial discharge and charge capacities are 208.3 and 194.1 mAh g^{-1}, respectively, corresponding to a Coulombic efficiency of 93.3%. Such an irreversible capacity loss in the initial cycle corresponds to formation of a solid electrolyte interface membrane. The plateau observed in the discharge process at about 2.75 V originates from the insertion of Li^+ into the $FeF_3{\cdot}0.33H_2O$ lattice (lithiation), which leads to formation of $Li_xFeF_3{\cdot}0.33H_2O$/rGO. Accordingly, such a lithiation process is also reflected by the cyclic voltammogram (CV) profiles presented in the inset of Figure 6.

DOI: 10.1021/acsami.8b08526
ACS Appl. Mater. Interfaces 2018, 10, 29505−29510

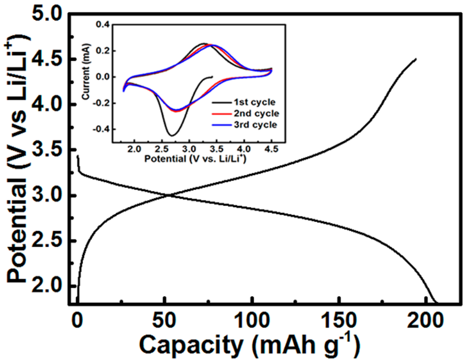

Figure 6. Initial charge and discharge curves of $FeF_3{\cdot}0.33H_2O$/rGO at 100 mA g^{-1}. Inset: CV curves for the initial three cycles at a scan rate of 0.1 mV s^{-1}.

The cycling charge−discharge performance of $FeF_3{\cdot}0.33H_2O$/rGO and the unsupported $FeF_3{\cdot}0.33H_2O$ NPs and the Coulombic efficiency of $FeF_3{\cdot}0.33H_2O$/rGO at 100 mA g^{-1} are presented in Figure 7a. Specifically, the discharge capacity gradually increases from 177.8 to 193.4 mA g^{-1} during the first 10 cycles. Remarkably, after 100 cycles, the $FeF_3{\cdot}0.33H_2O$/rGO sample maintains a discharge capacity of 172.3 mAh g^{-1}. In other words, a high capacity retention of 96.7% is achieved. In contrast, the unsupported $FeF_3{\cdot}0.33H_2O$ NPs exhibit much lower discharge capacities throughout the whole analysis range. The differential capacities of $FeF_3{\cdot}0.33H_2O$/rGO (mAh g^{-1} V^{-1}) in different cycles, from the 1st to 100th, are plotted as a function of cell potential (V vs Li/Li^+) in Figure 7b. The nearly identical peaks from the 10th to 100th cycle show clear evidence of great cycle stability.

To reveal the impact of the $FeF_3{\cdot}0.33H_2O$−rGO interfacial interactions on the electrochemical properties, the cycling charge−discharge performance evolutions of both $FeF_3{\cdot}0.33H_2O$/rGO and the unsupported $FeF_3{\cdot}0.33H_2O$ NPs were tested and compared under identical experimental conditions with a current density of 100 mA g^{-1}. Specifically, $FeF_3{\cdot}0.33H_2O$/rGO presents a stable discharge capacity of 133.1 mAh g^{-1} after 100 cycles, while the discharge capacity of unsupported NPs fades significantly, decreasing from 120 to 84.2 mAh g^{-1} with merely less than 70% of its initial capacity retained (see Figure 7c). This set of results strongly suggests that the formation of $FeF_3{\cdot}0.33H_2O$−rGO interfacial bonds not only boosts the absolute value of the initial discharge capacity of the $FeF_3{\cdot}0.33H_2O$ NPs by 147.8 mAh g^{-1} but also greatly enhances the cyclic stability of the $FeF_3{\cdot}0.33H_2O$ NPs by as much as 58% seen in the 100th cycle.

The rate cycling performance of $FeF_3{\cdot}0.33H_2O$/rGO and the unsupported $FeF_3{\cdot}0.33H_2O$ NPs as current density varies, from 100 to 2000 mA g^{-1}, is plotted in Figure 7d. Other than its excellent capacity retention, $FeF_3{\cdot}0.33H_2O$/rGO further demonstrates great rate performance. Overall, $FeF_3{\cdot}0.33H_2O$/rGO exhibits greater rate capacity at all current densities. Specifically, the capacity of $FeF_3{\cdot}0.33H_2O$/rGO remains 85.5 mAh g^{-1} at 2000 mA g^{-1}, while at the same current density, the unsupported $FeF_3{\cdot}0.33H_2O$ NPs deliver merely 66.0 mAh g^{-1}. Moreover, after 50 cycles, the capacity of $FeF_3{\cdot}0.33H_2O$/rGO is restored to 178.6 mAh g^{-1} at 100 mA g^{-1}, exhibiting greatly enhanced electrochemical stability.

EIS experiments were performed to investigate the kinetics of Li^+ intercalation into $FeF_3{\cdot}0.33H_2O$/rGO. Figure 8 shows the Nyquist plots of $FeF_3{\cdot}0.33H_2O$/rGO before electrochemical cycling and after different cycles at a charge state of 3.3 V. Generally, each Nyquist curve features (1) a semicircle in the high-frequency region and (2) an inclined line in the low-frequency region. The semicircle is tightly associated with the charge-transfer process with the charge-transfer resistance (R_{ct}) being the diameter of the semicircle, while the inclined

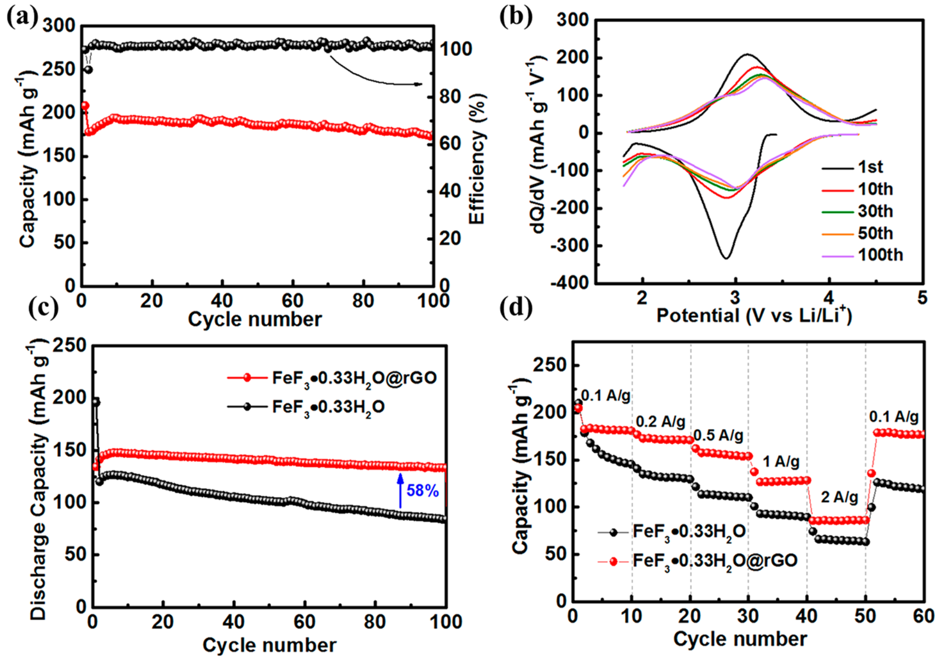

Figure 7. (a) Cycling charge−discharge performance of $FeF_3{\cdot}0.33H_2O$/rGO and the unsupported $FeF_3{\cdot}0.33H_2O$ NPs and the Coulombic efficiency of $FeF_3{\cdot}0.33H_2O$/rGO at 100 mA g^{-1} in 100 cycles; (b) Differential capacity of $FeF_3{\cdot}0.33H_2O$/rGO in different cycles; (c) Cycling charge−discharge performance evolution of $FeF_3{\cdot}0.33H_2O$/rGO and the unsupported $FeF_3{\cdot}0.33H_2O$ NPs in 100 cycles at 500 mA g^{-1}; (d) Discharge capacity evolution of $FeF_3{\cdot}0.33H_2O$/rGO and the unsupported $FeF_3{\cdot}0.33H_2O$ NPs as charge and discharge rates vary.

DOI: 10.1021/acsami.8b08526
ACS Appl. Mater. Interfaces 2018, 10, 29505−29510

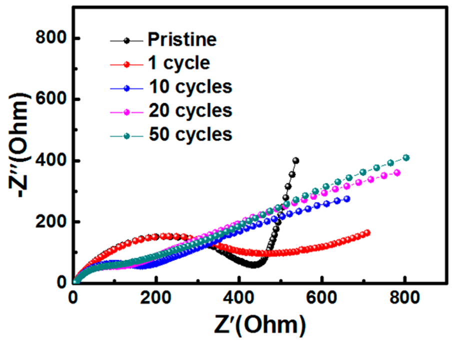

Figure 8. Nyquist plots of the $FeF_3 \cdot 0.33H_2O$/rGO nanocomposites after different cycles at a current density of 100 mA g^{-1}. The Nyquist plot of pristine $FeF_3 \cdot 0.33H_2O$/rGO before any tests is also plotted for comparison.

line is correlated to the diffusion of Li^+ in the electrode structures. In Figure 8, the R_{ct} regression after 10 cycles can be attributed to further reduction of rGO during the Li^+ intercalation/deintercalation process. Moreover, the Nyquist plots do not show detectable difference after 10 cycles. This is additional strong evidence of a stable interface between the active material and electrolyte.

Parallel calorimetric, structural, and computational studies are being carried out by our team to investigate the interfacial bonding energetics, specific bonds, and atomic-scale model for this $FeF_3 \cdot 0.33H_2O$/rGO nanocomposite system. The results will be reported separately in our subsequent publications.

■ CONCLUSION

In summary, high loading of the $FeF_3 \cdot 0.33H_2O$ NPs on rGO sheets was achieved using an in situ approach. A discharge capacity of ~208.3 mAh g^{-1} was recorded at 0.5 C. The $FeF_3 \cdot 0.33H_2O$/rGO nanocomposite exhibits excellent cycle capability with a highly reversible discharge capacity of 133.1 mAh g^{-1} after 100 cycles at 1000 mA g^{-1}, and the capacity retention is about 97%. Such outstanding electrochemical and rate performance are attributed to improved conductivity and minimized particle aggregation owing to the enhanced $FeF_3 \cdot 0.33H_2O$ NP−rGO sheet interfacial bonding. This work provides encouraging experimental evidence and an alternative strategy suggesting that iron fluoride−carbon nanocomposites could serve as cathode materials for LIBs with enhanced performance and stability.

■ AUTHOR INFORMATION

Corresponding Authors

*E-mail: junlu@anl.gov.
*E-mail: d.wu@wsu.edu.

ORCID

Liangjie Fu: 0000-0002-9761-5305
Jun Lu: 0000-0003-0858-8577
Di Wu: 0000-0001-6879-321X

Notes

The authors declare no competing financial interest.

■ ACKNOWLEDGMENTS

This work was supported by institutional funds from the Gene and Linda Voiland School of Chemical Engineering and Bioengineering at Washington State University. J. L. gratefully acknowledges support from the U.S. Department of Energy (DOE), Office of Energy Efficiency and Renewable Energy, Vehicle Technologies Office. Argonne National Laboratory is operated for DOE Office of Science by UChicago Argonne, LLC, under contract number DE-AC02-06CH11357.

■ REFERENCES

(1) Larcher, D.; Tarascon, J. M. Towards Greener and More Sustainable Batteries for Electrical Energy Storage. *Nat. Chem.* **2015**, *7*, 19−29.

(2) Goodenough, J. B.; Park, K. S. The Li-Ion Rechargeable Battery: A Perspective. *J. Am. Chem. Soc.* **2013**, *135*, 1167−1176.

(3) Weng, G.; Su, Y.; Liu, Z. Q.; Wu, Z. Y.; Chen, S.; Zhang, J. H.; Xu, C. W. Synthesis and Properties of Copolymer of 3-Thienylmethyl Disulfide and Benzyl Disulfide for Cathode Material in Lithium Batteries. *J. Appl. Polym. Sci.* **2010**, *116*, 727−735.

(4) Liu, W.; Oh, P.; Liu, X.; Lee, M. J.; Cho, W.; Chae, S.; Kim, Y.; Cho, J. Nickel-Rich Layered Lithium Transition-Metal Oxide for High-Energy Lithium-Ion Batteries. *Angew. Chem., Int. Ed.* **2015**, *54*, 4440−4458.

(5) Plitz, I.; Badway, F.; Al-Sharab, J.; DuPasquier, A.; Cosandey, F.; Amatucci, G. G. Structure and Electrochemistry of Carbon-Metal Fluoride Nanocomposites Fabricated by Solid-State Redox Conversion Reaction. *J. Electrochem. Soc.* **2005**, *152*, A307−A315.

(6) Cabana, J.; Monconduit, L.; Larcher, D.; Palacín, M. R. Beyond Intercalation-Based Li-Ion Batteries: The State of the Art and Challenges of Electrode Materials Reacting through Conversion Reactions. *Adv. Mater.* **2010**, *22*, E170−E192.

(7) Reddy, M. A.; Breitung, B.; Wall, C.; Trivedi, S.; Chakravadhanula, V. S.K.; Helen, M.; Fichtner, M. Facile Synthesis of Carbon-Metal Fluoride Nanocomposites for Lithium-Ion Batteries. *Energy Technol.* **2016**, *4*, 201−211.

(8) Wang, F.; Robert, R.; Chernova, N. A.; Pereira, N.; Omenya, F.; Badway, F.; Hua, X.; Ruotolo, M.; Zhang, R.; Wu, L.; Volkov, V.; Su, D.; Key, B.; Whittingham, M. S.; Grey, C. P.; Amatucci, G. G.; Zhu, Y.; Graetz, J. Conversion Reaction Mechanisms in Lithium Ion Batteries: Study of the Binary Metal Fluoride Electrodes. *J. Am. Chem. Soc.* **2011**, *133*, 18828−18836.

(9) Teng, Y. T.; Pramana, S. S.; Ding, J.; Wu, T.; Yazami, R. Investigation of the Conversion Mechanism of Nanosized CoF2. *Electrochim. Acta* **2013**, *107*, 301−312.

(10) Gu, W.; Borodin, O.; Zdyrko, B.; Lin, H. T.; Kim, H.; Nitta, N.; Huang, J.; Magasinski, A.; Milicev, Z.; Berdichevsky, G.; Yushin, G. Lithium-Iron Fluoride Battery with in Situ Surface Protection. *Adv. Funct. Mater.* **2016**, *26*, 1507−1516.

(11) Zhou, M.; Zhao, L.; Kitajou, A.; Okada, S.; Yamaki, J. I. Mechanism on Exothermic Heat of FeF 3 Cathode in Li-Ion Batteries. *J. Power Sources* **2012**, *203*, 103−108.

(12) Li, C.; Gu, L.; Tsukimoto, S.; Van Aken, P. A.; Maier, J. Low-Temperature Ionic-Liquid-Based Synthesis of Nanostructured Iron-Based Fluoride Cathodes for Lithium Batteries. *Adv. Mater.* **2010**, *22*, 3650−3654.

(13) Yamakawa, N.; Jiang, M.; Key, B.; Grey, C. P. Identifying the Local Structures Formed during Lithiation of the Conversion Material, Iron Fluoride, in a Li Ion Battery: A Solid-State NMR, X-Ray Diffraction, and Pair Distribution Function Analysis Study. *J. Am. Chem. Soc.* **2009**, *131*, 10525−10536.

(14) Shen, Y.; Wang, X.; Hu, H.; Jiang, M.; Yang, X.; Shu, H. A Graphene Loading Heterogeneous Hydrated Forms Iron Based Fluoride Nanocomposite as Novel and High-Capacity Cathode Material for Lithium/Sodium Ion Batteries. *J. Power Sources* **2015**, *283*, 204−210.

(15) Liao, P.; MacDonald, B. L.; Dunlap, R. A.; Dahn, J. R. Combinatorially Prepared $[LiF]_{1-x}Fe_x$ Nanocomposites for Positive Electrode Materials in Li-Ion Batteries. *Chem. Mater.* **2008**, *20*, 454−461.

(16) Liu, L.; Guo, H.; Zhou, M.; Wei, Q.; Yang, Z.; Shu, H.; Yang, X.; Tan, J.; Yan, Z.; Wang, X. A Comparison among $FeF_3 \cdot 3H_2O$, $FeF_3 \cdot 0.33H_2O$ and FeF_3 Cathode Materials for Lithium Ion Batteries:

Structural, Electrochemical, and Mechanism Studies. *J. Power Sources* **2013**, *238*, 501−515.

(17) Liu, L.; Zhou, M.; Wang, X.; Yang, Z.; Tian, F.; Wang, X. Synthesis and Electrochemical Performance of Spherical FeF_3/ACMB Composite as Cathode Material for Lithium-Ion Batteries. *J. Mater. Sci.* **2012**, *47*, 1819−1824.

(18) Lu, Y.; Wen, Z.; Jin, J.; Wu, X.; Rui, K. Size-Controlled Synthesis of Hierarchical Nanoporous Iron Based Fluoride and Its High Performances in Rechargeable Lithium Ion Batteries. *Chem. Commun.* **2014**, *50*, 6487−6490.

(19) Li, L.; Yu, Y.; Meng, F.; Tan, Y.; Hamers, R. J.; Jin, S. Facile Solution Synthesis of α-$FeF_3 \cdot 3H_2O$ Nanowires and Their Conversion to α-Fe2O3 Nanowires for Photoelectrochemical Application. *Nano Lett.* **2012**, *12*, 724−731.

(20) Liu, J.; Liu, W.; Ji, S.; Wan, Y.; Gu, M.; Yin, H.; Zhou, Y. Iron Fluoride Hollow Porous Microspheres: Facile Solution-Phase Synthesis and Their Application for Li-Ion Battery Cathodes. *Chem. - Eur. J.* **2014**, *20*, 5815−5820.

(21) Chu, Q.; Xing, Z.; Tian, J.; Ren, X.; Asiri, A. M.; Al-Youbi, A. O.; Alamry, K. A.; Sun, X. Facile Preparation of Porous FeF_3 Nanospheres as Cathode Materials for Rechargeable Lithium-Ion Batteries. *J. Power Sources* **2013**, *236*, 188−191.

(22) Kim, S.-W.; Seo, D.-H.; Gwon, H.; Kim, J.; Kang, K. Fabrication of FeF_3 Nanoflowers on CNT Branches and Their Application to High Power Lithium Rechargeable Batteries. *Adv. Mater.* **2010**, *22*, 5260−5264.

(23) Li, C.; Yin, C.; Gu, L.; Dinnebier, R. E.; Mu, X.; Van Aken, P. A.; Maier, J. An $FeF_3 \cdot 0.5H_2O$ Polytype: A Microporous Framework Compound with Intersecting Tunnels for Li and Na Batteries. *J. Am. Chem. Soc.* **2013**, *135*, 11425−11428.

(24) Ma, R.; Wang, M.; Tao, P.; Wang, Y.; Cao, C.; Shan, G.; Yang, S.; Xi, L.; Chung, J. C.Y.; Lu, Z. Fabrication of FeF_3 Nanocrystals Dispersed into a Porous Carbon Matrix as a High Performance Cathode Material for Lithium Ion Batteries. *J. Mater. Chem. A* **2013**, *1*, 15060−15067.

(25) Ma, D.; Cao, Z.; Wang, H.; Huang, X.; Wang, L.; Zhang, X. Three-Dimensionally Ordered Macroporous FeF_3 and Its in Situ Homogenous Polymerization Coating for High Energy and Power Density Lithium Ion Batteries. *Energy Environ. Sci.* **2012**, *5*, 8538−8542.

(26) Wang, H.; Maiyalagan, T.; Wang, X. Review on Recent Progress in Nitrogen-Doped Graphene: Synthesis, Characterization, and Its Potential Applications. *ACS Catal.* **2012**, *2*, 781−794.

(27) Wei, D.; Liu, Y.; Wang, Y.; Zhang, H.; Huang, L.; Yu, G. Synthesis of N-Doped Graphene by Chemical Vapor Deposition and Its Electrical Properties. *Nano Lett.* **2009**, *9*, 1752−1758.

(28) Liu, Y.; Liu, P.; Wu, D.; Huang, Y.; Tang, Y.; Su, Y.; Zhang, F.; Feng, X. Boron-Doped, Carbon-Coated SnO_2/Graphene Nanosheets for Enhanced Lithium Storage. *Chem. - Eur. J.* **2015**, *21*, 5617−5622.

(29) Atar, N.; Eren, T.; Yola, M. L.; Gerengi, H.; Wang, S. Fe@Ag Nanoparticles Decorated Reduced Graphene Oxide as Ultrahigh Capacity Anode Material for Lithium-Ion Battery. *Ionics* **2015**, *21*, 3185−3192.

(30) Atar, N.; Eren, T.; Yola, M. L. Ultrahigh Capacity Anode Material for Lithium Ion Battery Based on Rod Gold Nanoparticles Decorated Reduced Graphene Oxide. *Thin Solid Films* **2015**, *590*, 156−162.

(31) Li, B.; Rooney, D. W.; Zhang, N.; Sun, K. An in Situ Ionic-Liquid-Assisted Synthetic Approach to Iron Fluoride/Graphene Hybrid Nanostructures as Superior Cathode Materials for Lithium Ion Batteries. *ACS Appl. Mater. Interfaces* **2013**, *5*, 5057−5063.

(32) Jiang, M.; Wang, X.; Wei, S.; Shen, Y.; Hu, H. An Ionic-Liquid-Assisted Approach to Synthesize a Reduced Graphene Oxide Loading Iron-Based Fluoride as a Cathode Material for Sodium-Ion Batteries. *J. Alloys Compd.* **2016**, *670*, 362−368.

(33) Liu, J.; Wan, Y.; Liu, W.; Ma, Z.; Ji, S.; Wang, J.; Zhou, Y.; Hodgson, P.; Li, Y. Mild and Cost-Effective Synthesis of Iron Fluoride-Graphene Nanocomposites for High-Rate Li-Ion Battery Cathodes. *J. Mater. Chem. A* **2013**, *1*, 1969−1975.

(34) Zhao, X.; Hayner, C. M.; Kung, M. C.; Kung, H. H. Photothermal-Assisted Fabrication of Iron Fluoride-Graphene Composite Paper Cathodes for High-Energy Lithium-Ion Batteries. *Chem. Commun.* **2012**, *48*, 9909−9911.

(35) Wei, S.; Wang, X.; Liu, M.; Zhang, R.; Wang, G.; Hu, H. Spherical $FeF_3 \bullet 0.33H_2O$/MWCNTs Nanocomposite with Mesoporous Structure as Cathode Material of Sodium Ion Battery. *J. Energy Chem.* **2018**, *27*, 573−581.

(36) Chu, Q.; Xing, Z.; Ren, X.; Asiri, A. M.; Al-Youbi, A. O.; Alamry, K. A.; Sun, X. Reduced Graphene Oxide Decorated with FeF3 Nanoparticles: Facile Synthesis and Application as a High Capacity Cathode Material for Rechargeable Lithium Batteries. *Electrochim. Acta* **2013**, *111*, 80−85.

(37) Jung, H.; Song, H.; Kim, T.; Lee, J. K.; Kim, J. FeF_3 Microspheres Anchored on Reduced Graphene Oxide as a High Performance Cathode Material for Lithium Ion Batteries. *J. Alloys Compd.* **2015**, *647*, 750−755.